Structural mechanism of Necrocide 1 activation of human TRPM4 that triggers necrosis by sodium overload

Celso M. Teixeira-Duarte[1,2,#], Wan Fu[3,#], Weizhong Zeng[1,2], Jianghuang Wang[3], Xinzhe Jiang[3], Ziye Zhao[3], Qing Zhong[3,*] & Youxing Jiang[1,2,*]

Affiliations:

[1] Howard Hughes Medical Institute and Department of Physiology, University of Texas Southwestern Medical Center, Dallas, Texas, USA

[2] Department of Biophysics, University of Texas Southwestern Medical Center, Dallas, Texas, USA

[3] Institute for Translational Medicine on Cell Fate and Disease, Shanghai Ninth People's Hospital, Key Laboratory of Cell Differentiation and Apoptosis of National Ministry of Education, Department of Pathophysiology, Shanghai Jiao Tong University School of Medicine, Shanghai, China

[#] These authors contributed equally.

[*]Correspondence to:

Youxing Jiang, Ph.D., Department of Physiology, UT Southwestern Medical Center, 5323 Harry Hines Blvd., Dallas, Texas 75390-9040, Tel. 214 645-6027; Fax. 214 645-6042; E-Mail: youxing.jiang@utsouthwestern.edu

Qing Zhong, Ph.D., Department of Pathophysiology, Shanghai Jiao Tong University School of Medicine; Tel. 021-63846590-776429; E-Mail: qingzhong@shsmu.edu.cn

Abstract

The small molecule Necrocide 1 (NC1) constitutively activates human TRPM4, triggering Na^+ influx and leading to necrotic cell death, a process termed Necrosis by Sodium Overload (NECSO). NC1 activation is specific to human TRPM4 and does not affect most of the other mammalian TRPM4 orthologs. Here, we elucidate the molecular mechanism underlying NC1 activation and its species-specific selectivity for human TRPM4 using a combination of single-particle cryo-EM, electrophysiology, and cell death assays. We identify the NC1-binding site and the key molecular determinants responsible for channel activation. In addition, we explain the insensitivity of mouse TRPM4 to NC1 and pinpoint specific residues that define NC1 specificity for human TRPM4. Given the upregulation of TRPM4 in various human cancers, our mechanistic insights into NC1 activation and specificity provide a framework for the potential development of cancer therapeutics targeting TRPM4-mediated necrosis.

40 # Introduction

41 TRPM4 is a Ca^{2+}-activated, monovalent-selective cation channel belonging to the transient
42 receptor potential melastatin (TRPM) subfamily[1-3]. It is ubiquitously expressed[4] and plays a key
43 role in regulating various physiological processes, including cardiac conduction[5-8], immune
44 response[9], and cell death[10-14]. Notably, TRPM4 is upregulated in several cancer types[15], such as
45 prostate[16-18], breast[19,20], diffuse large B-cell lymphoma[21], and acute myeloid leukemia[22], making it
46 an attractive target for therapeutic intervention. Despite this potential, commonly used TRPM4
47 modulators suffer from low specificity[5,23-27], prompting extensive efforts to develop monoclonal
48 antibodies[28-31] and small molecules[32,33] specific for this channel. Among the latter, anthranilic acid
49 derivatives, CBA, NBA, and IBA, have emerged as promising inhibitors[32,34,35]. Recent structural
50 studies revealed that NBA and IBA bind in the vanilloid binding pocket, adjacent to the binding
51 sites of the exogenous modulator decavanadate and the endogenous ligand $PI(4,5)P_2$, to exert their
52 inhibitory effects[27,35,36].

53 TRPM4 is activated by intracellular calcium and $PI(4,5)P_2$, promoting membrane
54 depolarization via monovalent cation influx[1,23]. Interestingly, TRPM4 channel opening has been
55 implicated in necrotic cell death triggered by anticancer treatments in human breast cancer cells[12].
56 Necrocide 1 (NC1) ((S')-3-cycloheptyl-3-(4-hydroxyphenyl)-6-methoxy-7-methyl-1,3-
57 dihydroindole-2-one) is a small molecule derived from the optimization of a compound identified
58 in a screen for anti-tumorigenic activity[37,38]. NC1 induces necrotic cell death in several cancer cell
59 lines, including PC-3 (prostate) and MCF-7 (breast), and has been shown to suppress tumor growth
60 in human cancer xenografts[39]. Importantly, NC1 does not trigger necrosis in non-tumorigenic cells
61 such as fibroblasts and umbilical vein endothelial cells[39].

62 Recent findings demonstrate that NC1 induces necrotic cell death by directly activating
63 human TRPM4, triggering Na^+ influx that leads to osmotic swelling and membrane rupture, a
64 process termed Necrosis by Sodium Overload (NECSO)[40,41]. Interestingly, NC1 exhibits a high
65 degree of species specificity: it activates human TRPM4 but not most other mammalian TRPM4
66 orthologues or other human TRPM family members. Since evading apoptosis is a hallmark of
67 cancer cells[42,43], targeting alternative, non-apoptotic pathways such as TRPM4-mediated necrosis
68 may offer novel therapeutic avenues. Understanding the molecular mechanism of NC1-induced

human TRPM4 activation and its species specificity is therefore critical for the rational development of TRPM4-targeted anticancer therapies.

In this study, we combine single-particle cryo-EM, electrophysiology, and cell death assays to elucidate the structural mechanism by which NC1 activates human TRPM4. We demonstrate that NC1 functions as a non-competitive surrogate of the endogenous Ca^{2+} ligand – it binds to a pocket within the S1-S4 domain adjacent to the Ca^{2+} site and induces the same conformational changes as those triggered by Ca^{2+}. Like Ca^{2+}-mediated activation, NC1-induced channel opening also requires membrane $PI(4,5)P_2$ to stabilize the open state. Through comparative mutagenesis and structural analysis of human and mouse TRPM4, we identify the molecular determinants of NC1 specificity. Our results reveal that the insensitivity of mouse TRPM4 to NC1 arises not from a lack of binding, but from drug-induced conformational changes that destabilize the selectivity filter and inactivate the channel. We identify three critical residues that confer NC1 sensitivity, and their substitution renders mouse TRPM4 responsive to NC1, offering insights into the species selectivity of NC1 and paving the way for future therapeutic development.

Results

NC1 activates hTRPM4 and promotes cell death

The small molecule Necrocide 1 (NC1) was recently shown to induce necrotic cell death by activating the human TRPM4 (hTRPM4) channel[40]. The key electrophysiological features of NC1-activated hTRPM4 were characterized using whole-cell patch-clamp recordings of hTRPM4-expressing HEK293 cells (Methods). NC1 activates TRPM4 slowly, requiring about two minutes for the current to reach its maximum, indicating a slow on-rate of NC1 binding (Fig. 1a and 1b). Most channels remain activated even after several minutes of washout, suggesting high-affinity binding and an extremely slow off-rate. With the presence of 1 mM EGTA in the pipette solution (cytosolic side), our recording conditions eliminate the potential contribution to channel activation from cytosolic Ca^{2+}, the endogenous ligand of TRPM4, confirming the Ca^{2+}-independence of NC1 activation.

To complement electrophysiological data, we conducted cell death and viability assays to assess hTRPM4-dependent necrosis in HeLa cells (Methods). While HeLa cells are insensitive to

98 NC1 due to a lack of detectable endogenous TRPM4, they become susceptible to NC1-induced
99 necrosis upon transient or stable expression of hTRPM4. In the cell death assay, EGFP-tagged
100 hTRPM4 was transiently expressed in HeLa cells, and necrotic morphology, characterized by
101 'balloon-like' cell swelling, was observed 24 hours after NC1 treatment (Fig. 1c). No necrosis was
102 observed in the NC1-treated control cells transiently expressing EGFP or EGFP-tagged mouse
103 TRPM4. This assay provides a qualitative readout of hTRPM4-dependent necrosis, enabling the
104 screening of mutational effects on the NC1 sensitivity of the channel, as discussed later. In the cell
105 viability assay, hTRPM4 was stably expressed in HeLa cells. Following 24-hour NC1 treatment
106 at varying concentrations, cytotoxicity was assessed by measuring intracellular ATP levels,
107 indicative of cell viability, using the CellTiter-Glo (CTG) assay (Fig. 1d, Methods). This assay
108 provides a quantitative measure of NC1's dose-dependent toxicity in hTRPM4-expressing cells.

109

110 **Structure of NC1-bound TRPM4**

111 To elucidate the structural basis of NC1 binding and its activation mechanism, we purified
112 detergent-solubilized hTRPM4 and determined its structure in complex with NC1 at 2.7 Å
113 resolution using single-particle cryo-EM (Fig. 2a, Supplementary Fig. 1a, Supplementary Table 1,
114 and Methods). The NC1 ligand is unambiguously resolved in the EM density map (Fig. 2b).
115 Occupying a pocket within the S1–S4 domain just above the Ca^{2+} activation site, NC1 forms
116 extensive hydrophobic and hydrogen-bonding interactions with surrounding residues (Fig. 2b).

117 To validate NC1 binding, we performed mutagenesis of residues interacting with the ligand.
118 Due to the extensive contact surface between NC1 and its binding pocket, single-alanine
119 substitutions were insufficient to disrupt NC1 binding and channel activation (Supplementary Fig.
120 2a). We therefore introduced bulkier tryptophan substitutions to block NC1 access sterically.
121 Among all tested, three hTRPM4 single-tryptophan mutants - Y790W, L824W, and I909W –
122 completely lost sensitivity to NC1 (Fig. 2c and 2d). These mutants remained responsive to
123 Ca^{2+}/PI(4,5)P_2 activation, particularly I909W (Supplementary Fig. 2b), confirming that these
124 mutations prevent NC1 binding while retaining native activation. The loss of NC1 activation in
125 these mutants was further supported by cell viability assays using stable HeLa cell lines expressing
126 either wild-type or mutant hTRPM4. While NC1 treatment induced a dose-dependent loss of

127 viability in WT-expressing cells, the mutant-expressing cells were resistant to NC1-induced
128 necrosis (Fig. 2e).

129 Despite robust NC1 activation observed in functional assays, the NC1-bound TRPM4
130 structure adopts a conformation intermediate between the closed and open states, when compared
131 to previously determined apo (closed) and Ca^{2+}/PI(4,5)P_2-bound (open) structures (Fig. 3a and
132 Supplementary Fig. 3a). NC1 binding induces local conformational changes in the S1-S4 domain
133 resembling those triggered by Ca^{2+} (Fig. 3b and Supplementary Fig. 3b); however, the channel
134 pore and the cytosolic domains remain in a closed conformation (Fig. 3a, 3c, 3d, and
135 Supplementary Fig. 3a). Within S1-S4, NC1 binding causes the S3 helix to shift inward toward
136 the NC1-binding pocket, moving the W864 side chain closer to the C-terminal end of S4 (Fig. 3b).
137 Through tight packing with H908 on S4, W864 motion displaces the C-terminal part of S4 toward
138 S5 in the adjacent pore domain (Fig. 3b). In the apo TRPM4 structure, F910 at the C-terminal part
139 of S4 forms a key contact with F935 near the cytosolic end of S5 - a coupling essential for
140 transducing Ca^{2+}-induced movements into pore opening, as shown in the Ca^{2+}/PI(4,5)P_2-bound
141 structure[36] (Fig. 3e). In contrast, the NC1-bound structure shows disordered side chains for both
142 F910 and F935, indicating a loss of this critical contact (Fig. 3e). These structural features of NC1-
143 bound hTRPM4, including an activated S1-S4 domain, a closed pore, and disrupted F910–F935
144 coupling, mirror the Ca^{2+}-bound hTRPM4 structure in the absence of PI(4,5)P_2, previously
145 proposed to represent a desensitized state[36] (Fig 3e and Supplementary Fig. 3c). Since PI(4,5)P_2
146 binding is required to stabilize the open state upon Ca^{2+} activation[36], the resemblance between
147 NC1- and Ca^{2+}-bound structures suggests that NC1 triggers local conformational changes similar
148 to those induced by Ca^{2+} and also relies on PI(4,5)P_2 binding to stabilize the open channel.

149

150 **PI(4,5)P_2-dependent NC1 activation of hTRPM4**

151 To test whether PI(4,5)P_2 is indeed required for NC1 activation, we performed patch-clamp
152 recordings of hTRPM4-expressing HEK293 cells in the inside-out configuration. Following initial
153 activation by cytosolic Ca^{2+}, TRPM4 undergoes desensitization to a steady-state level with reduced
154 open probability due to depletion of membrane PI(4,5)P_2, caused by Ca^{2+}-induced phospholipase
155 C activation[44,45] (Fig. 4a). This loss of PI(4,5)P_2 after Ca^{2+} activation creates a condition suitable
156 for assessing NC1 activation in the absence of PI(4,5)P_2. Indeed, hTRPM4 becomes unresponsive

157 to NC1 following PI(4,5)P_2 depletion (Fig. 4a). While PI(4,5)P_2 alone cannot activate TRPM4, its
158 addition in the presence of NC1 robustly activates the channel, restoring current to the pre-
159 desensitization level (Fig. 4a). Consistent with whole-cell recordings, NC1 activates TRPM4
160 slowly in the presence of PI(4,5)P_2, and the ligand remains tightly bound, making it difficult to
161 wash out (Fig. 4b). These results indicate that PI(4,5)P_2 is a prerequisite for NC1-induced
162 activation of hTRPM4.

163 To further support this conclusion, we mutated key positively charged PI(4,5)P_2-interacting
164 residues, R664A, K925A, and K928A, previously identified in the Ca^{2+}/PI(4,5)P_2-activated
165 TRPM4 structure[36]. With surface expression levels comparable to the wild-type channel
166 (Supplementary Fig. 4a), these mutations significantly impaired NC1 activation in whole-cell
167 recordings, with much stronger effects on inward currents at negative potentials (Fig. 4c and 4d).
168 Additionally, HeLa cells overexpressing these mutants were no longer sensitive to NC1-induced
169 cell death, further validating the requirement of PI(4,5)P_2 for NC1-mediated TRPM4 activation
170 (Supplementary Fig. 4b).

171 The PI(4,5)P_2 dependence of NC1-induced hTRPM4 activation was further confirmed by
172 determining the structure of the channel bound to both PI(4,5)P_2 and NC1 at 2.8 Å resolution (Fig.
173 5a and 5b, Supplementary Fig. 1b, Supplementary Table 1, and Methods). In this structure,
174 hTRPM4 adopts an open conformation virtually identical to that of the Ca^{2+}/PI(4,5)P_2-activated
175 channel (Fig. 5a). Compared to the structure with NC1 alone, the presence of PI(4,5)P_2 enables
176 the NC1-induced conformational changes within the S1-S4 domain to be effectively transmitted
177 to the pore through the reformation of the critical F910/F935 contact, thereby leading to pore
178 opening (Fig. 3c and 3d and Fig. 5c and 5d). This pore-opening movement is further coupled to
179 large-scale rotational and upward swinging motions of the cytosolic domains via the TRP domain,
180 as also observed in the Ca^{2+}/PI(4,5)P_2-activated structure[36] (Fig. 5c and 5e). Interestingly, despite
181 no exogenous Ca^{2+} being added, the canonical Ca^{2+}-binding site within the S1-S4 domain is
182 occupied by a Ca^{2+} ion in the NC1/PI(4,5)P_2-bound structure (Fig. 5b). The stabilized, active
183 conformation of S1-S4 induced by NC1 and PI(4,5)P_2 likely increases the apparent Ca^{2+} affinity,
184 allowing residual micromolar Ca^{2+} in nominally Ca^{2+}-free conditions to bind. To confirm that Ca^{2+}
185 is not required for channel opening in the NC1/PI(4,5)P_2-bound structure, we also determined the
186 structure of the complex prepared in the presence of EGTA (Supplementary Fig. 1c,

187 Supplementary Table 1, and Methods). In this case, no bound Ca^{2+} is observed, yet the channel
188 remains in the same open conformation, confirming that NC1 and $PI(4,5)P_2$ are sufficient to
189 activate the channel independently of Ca^{2+} (Supplementary Fig. 5a and 5b). Furthermore, the
190 presence of Ca^{2+} does not appear to exert any potentiating effect on NC1 activation, as
191 NC1/$PI(4,5)P_2$-activated currents are comparable when recorded in both the absence and presence
192 of Ca^{2+} (Supplementary Fig. 5c).

193 Together, these structural and functional results reveal several key insights into $PI(4,5)P_2$-
194 dependent NC1 activation: NC1 induces conformational changes in the S1-S4 domain similar to
195 those triggered by Ca^{2+} without interfering with Ca^{2+} binding; Like Ca^{2+}, NC1 alone stabilizes the
196 channel in a desensitized state, requiring $PI(4,5)P_2$ to promote channel opening; In the presence of
197 $PI(4,5)P_2$, both NC1 and Ca^{2+} can independently activate hTRPM4.

198

199 **Molecular determinants of NC1 specificity for human TRPM4**

200 NC1 activates human but not mouse TRPM4[40], despite the high sequence and structural
201 homology between the two orthologs. This species-specific activation is particularly intriguing
202 given the identical amino acid composition and conserved structure of the NC1-binding pocket.
203 To identify the molecular determinants underlying this specificity, we used the cell death assay to
204 screen various mutations in both human and mouse TRPM4 expressed in HeLa cells. Through a
205 combination of chimeric constructs and point mutations (Supplementary Fig. 6, Supplementary
206 Fig. 7, and associated legends), we identified three residues that potentially contribute to the
207 selective activation of hTRPM4 by NC1: V904 on the S4 helix (corresponding to L900 in
208 mTRPM4), P997 in the pore domain (R993 in mTRPM4), and R1064 on the TRP helix (S1060 in
209 mTRPM4) (Fig. 6a).

210 We next tested whether mouse TRPM4 could be converted into an NC1-sensitive channel
211 by introducing single, double, and triple mutations in which the three residues (L900, R993, and
212 S1060) were replaced with their human TRPM4 counterparts. Figure 6b and Figure 6c show the
213 whole-cell patch-clamp recordings of NC1 activation in these mutants. Strikingly, the single
214 S1060R mutation in mTRPM4 was sufficient to confer NC1 sensitivity; however, the resulting
215 current was outwardly rectifying, with greater conductance at depolarized membrane potentials.

216 In contrast, mTRPM4 mutants bearing L900V and/or R993P substitutions remained insensitive to
217 NC1 when tested individually or in combination. Notably, when these mutations were combined
218 with S1060R, NC1 sensitivity was significantly enhanced. The mTRPM4 triple mutant
219 (L900V/R993P/S1060R) displayed an NC1 activation profile nearly identical to that of hTRPM4.
220 As these mutations do not target the Ca^{2+}- or PI(4,5)P_2-binding sites, they are not expected to affect
221 Ca^{2+}/PI(4,5)P_2-mediated activation of mTRPM4. To test that, we measured Ca^{2+}/PI(4,5)P_2-
222 activated currents for all of these mutants using inside-out patch recordings and compared their
223 sensitivity to NC1/PI(4,5)P_2 activation (Supplementary Fig. 8a and 8b). The results show that all
224 mutants produced Ca^{2+}/PI(4,5)P_2-elicited currents comparable to those of wild-type mTRPM4,
225 indicating similar channel expression levels between the mutants and the WT. However, only
226 mutants containing the S1060R mutation could be partially (single and double mutants) or fully
227 (triple mutant) activated by NC1/PI(4,5)P_2, consistent with the observations from the whole-cell
228 recordings. Complementing these gain-of-function experiments, we also tested loss-of-function
229 mutations in hTRPM4 (Supplementary Fig. 8c and 8d). Consistent with the mTRPM4 mutagenesis
230 findings, mutations at V904 and P997 did not affect NC1 activation of hTRPM4. In contrast, both
231 the single R1064S mutation and the V904L/P997R/R1064S triple mutation significantly reduced
232 NC1 activation, though not completely abolishing it.

233 In addition, we generated the HeLa stable cell lines expressing those mTRPM4 gain-of-
234 function mutants and measured their viability in response to NC1 treatment (Fig. 6d). Consistent
235 with our electrophysiology result, expressing mTRPM4 with L900V and R993P mutations has
236 little effect on cell viability similar to control cells expressing WT mTRPM4 or empty vector;
237 however, the expression of S1060R single mutant or S1060R-containing double or triple mutants
238 progressively decreases the cell viability in response to NC1; cells expressing the
239 L900V/R993P/S1060R triple mutant of mTRPM4 exhibit similar sensitivity to NC1-induced
240 necrosis as hTRPM4-expressing cells.

241

242 **The structural basis of NC1 specificity**

243 To gain structural insight into the NC1 specificity of TRPM4, we determined the cryo-EM
244 structures of both the NC1-insensitive WT mTRPM4 and its NC1-activated
245 L900V/R993P/S1060R triple mutant, each in the presence of NC1 (Supplementary Fig. 9,

246 Supplementary Table 2, and Methods). As PI(4,5)P_2 is required for NC1 activation in hTRPM4, it
247 was also included during mTRPM4 protein preparation (Methods).

248 The structure of WT mTRPM4 in the presence of NC1 and PI(4,5)P_2 was resolved at 2.9
249 Å resolution (Fig. 7a). Surprisingly, NC1 still binds to mTRPM4 at the same pocket as in hTRPM4
250 with identical surrounding residues (Fig. 7b), despite failing to activate the channel. Relative to
251 the apo mTRPM4 structure, NC1 binding induces similar local conformational changes within the
252 S1-S4 domain, as observed in hTRPM4 (Supplementary Fig. 10a). However, unlike
253 NC1/PI(4,5)P_2-activated hTRPM4, where large swinging and rotational movements of the
254 cytosolic domains are coupled to pore opening, the cytosolic domains of NC1/PI(4,5)P_2-bound
255 mTRPM4 closely resemble the apo closed conformation, with only a subtle rigid-body shift (Fig.
256 7a). Notably, three distinct conformational changes in the transmembrane region of
257 NC1/PI(4,5)P_2-bound mTRPM4 distinguish it from the NC1-sensitive hTRPM4 and likely
258 underlie its lack of activation (Fig. 7c, 7d and 7e). Firstly, the entire S1-S4 domain moves laterally
259 toward the center of the channel (Fig. 7c). Secondly, the central filter and surrounding pore helices
260 exhibit no clear density, suggesting the filter becomes disordered upon NC1 binding (Fig. 7d) - a
261 surprising finding, as this tightly packed central filter region remains steady during channel gating
262 and is typically the best-resolved in TRPM4 structures. Thirdly, the S5 helix shifts inward toward
263 the filter, while the pore-lining S6 helix moves outward, widening the intracellular gate (Fig. 7c
264 and 7e).

265 The latter two structural changes appear to originate from the lateral movement of S1-S4.
266 Due to tight S5-mediated packing between the S1-S4 domain and the neighboring subunit's pore
267 domain, this lateral shift of S1-S4 drives S5 inward, compressing the adjacent pore helix and filter
268 toward the central axis (Fig. 7c). Unable to accommodate this compression, the filter likely
269 undergoes a promiscuous movement and adopts a disordered, non-conductive conformation,
270 leading to the collapse of the ion conduction pathway. The accompanying outward motion of S6
271 likely serves to relieve the spatial strain caused by the rearrangement of the central pore.
272 Importantly, these conformational changes are solely induced by NC1 binding, as an NC1-bound
273 mTRPM4 structure prepared without PI(4,5)P_2 is identical to the NC1/PI(4,5)P_2-bound form
274 (Supplementary Fig. 9b, Supplementary Fig. 10b, Supplementary Table 2, and Methods). Thus,
275 the insensitivity of mTRPM4 to NC1 activation is not due to a lack of drug binding, but rather to

276 NC1-induced collapse of the selectivity filter, rendering the channel non-conductive, analogous to
277 C-type inactivation observed in certain K^+ channels[46].

278 We next determined the structure of the NC1-sensitive mTRPM4 triple mutant
279 (L900V/R993P/S1060R) in complex with NC1 and PI(4,5)P_2 (Fig. 7f, Supplementary Fig. 9c,
280 Supplementary Table 2, and Methods). Unlike WT mTRPM4, the mutant's pore domain is well
281 structured and adopts an open conformation (Fig. 7e), and its S1-S4 domain no longer undergoes
282 a lateral movement. The overall structure of the mutant closely resembles that of the
283 NC1/PI(4,5)P_2-bound open hTRPM4 (Supplementary Fig. 10c), faithfully recapitulating the
284 activation mechanism observed in the human channel. Given that the S1060R mutation in the TRP
285 helix is the key determinant for conferring NC1 sensitivity, we focused our structural comparison
286 on this region between NC1/PI(4,5)P_2-bound WT and mutant mTRPM4. In the mutant, R1060
287 forms a network of inter-domain interactions absent in the WT channel (Fig. 7g). Specifically,
288 R1060 mediates a cluster of salt bridges and hydrogen bonds involving D858 and W860 at the N-
289 terminus of S3, as well as the glycerol phosphate head group of PI(4,5)P_2. These interactions serve
290 to stabilize the S1-S4 domain, preventing the inward lateral movement observed in NC1-bound
291 WT mTRPM4 that disrupts the pore. Notably, this arginine residue, crucial for NC1 sensitivity, is
292 conserved in human and primate TRPM4 orthologs but is replaced by a serine in most other
293 mammalian species.

294

295 ## Discussion

296 The small molecule NC1 activates hTRPM4, triggering Na^+ influx and leading to necrotic
297 cell death via sodium overload. Through structural and functional analyses, we elucidated the
298 molecular mechanism underlying NC1-mediated activation of hTRPM4. NC1 binds near the Ca^{2+}
299 activation site within the S1-S4 domain and induces local conformational changes that mirror those
300 caused by Ca^{2+}. Like Ca^{2+}, NC1 requires membrane PI(4,5)P_2 to stabilize the open channel
301 conformation. Thus, NC1 acts as a non-competitive surrogate of the native ligand. NC1 engages
302 in extensive hydrophobic and polar interactions with surrounding residues, resulting in high-
303 affinity binding. Its binding site, deeply buried within the protein, likely contributes to its slow
304 activation kinetics and poor washout. The NC1 binding site is similar to that of the TRPM4
305 modulator deacetyl bisacodyl (DAB)[47] and to some modulator-binding pockets in TRPM3 (e.g.,

306 primidone and CIM 0216)[48,49] and TRPM8 (e.g., N-(3-aminopropyl)-2-[(3-
307 methylphenyl)methoxy]-N-[(thiophen-2-yl)methyl]benzamide (AMTB), cryosim-3 (C3), icilin,
308 and the menthol analog WS-12)[50-52].

309 NC1 selectively activates human TRPM4 but not most other mammalian TRPM4 orthologs.
310 Through comparative studies of human and mouse TRPM4, we determined that the species
311 specificity of NC1 activation is not due to a failure in drug binding. Instead, in mTRPM4, NC1
312 binding destabilizes the selectivity filter, rendering the channel non-conductive, akin to C-type
313 inactivation observed in certain K^+ channels. We identified R1064, located on the TRP helix of
314 hTRPM4, as a key determinant of NC1 specificity. This arginine mediates a network of
315 interdomain interactions that stabilize the S1-S4 domain's lateral position within the membrane.
316 In TRPM4s from mice and most other mammals, a serine occupies this position. The absence of
317 arginine-mediated stabilization permits a lateral shift of the S1-S4 domain upon NC1 binding,
318 which collapses the selectivity filter and inactivates the channel. Interestingly, akin to NC1, the
319 TRPM4 modulator CBA was shown to inhibit the human but not the mouse channel[34] and does
320 not exert any effect on other TRPM channel subfamily members[32]. However, the mechanistic
321 details that confer TRPM4 species-specificity to this compound have not been thoroughly explored.

322 The mechanistic insights into NC1 activation of hTRPM4 and its remarkable specificity
323 revealed in this study establish a structural framework for understanding how small molecules can
324 selectively modulate TRPM4 function. The defined NC1-binding mode provides an essential
325 molecular basis for rational drug design aimed at exploiting TRPM4-mediated necrosis as a
326 potential therapeutic avenue for cancer treatment.

327 The discovery that NC1 binds to an identical site in both human and mouse TRPM4
328 orthologs but induces markedly different functional outcomes emphasizes the structural subtleties
329 governing allosteric coupling and species-dependent channel gating. Given the widespread
330 reliance on murine and other mammalian models in preclinical studies, our findings underscore
331 the necessity of validating compound efficacy and mechanism in human-derived systems to ensure
332 accurate interpretation of pharmacological responses. This cross-species discrepancy also serves
333 as a cautionary example for drug development pipelines targeting ion channels, in which even
334 small structural variations can yield divergent functional consequences. Collectively, our results

335 provide a comprehensive molecular foundation for future high-throughput screening, structure-
336 guided optimization, and in vivo evaluation of TRPM4 modulators.

337 # Methods

338 **Protein expression and purification**

339 Full-length wild-type human TRPM4 (UniProtKB: Q8TD43) containing an N-terminal FLAG-tag
340 (DYKDDDDK) and full-length wild-type or L900V;R993P;S1060R mouse TRPM4 (UniprotKB:
341 Q7TN37) containing a C-terminal FLAG-tag were cloned into a pEZT-BM plasmid[53]. *E.coli*
342 DH10Bac cells were used to synthesize the bacmid that was employed in baculovirus production
343 in Sf9 cells (Thermo Fisher Scientific) using Cellfectin II reagent (Thermo Fisher Scientific). For
344 protein expression, HEK293S GnTI$^-$ cells (American Type Culture Collection (ATCC), CRL-3022)
345 grown in suspension to a density of $3x10^6$ cells/mL were infected with P3 viruses at a ratio of 1:40
346 (virus:cell, v/v) and supplemented with 10 mM sodium butyrate to boost protein expression. The
347 cells were then incubated at 37 °C for 48 h before being harvested by centrifugation (5000 g, 15
348 min, 4 °C). The cell pellet was resuspended in lysis buffer (50 mM Tris-HCl pH 7.5, 150 mM
349 NaCl) supplemented with protease inhibitors (0.5 µg/ml pepstatin, 2 µg/ml leupeptin, 1 µg/ml
350 aprotinin, and 1 mM PMSF) and homogenized by sonication. TRPM4 was then extracted with 1 %
351 (w/v) lauryl maltose neopentyl glycol (LMNG, Anatrace) in gentle agitation for 2 h at 4 °C. The
352 supernatant was subsequently collected by centrifugation (40000 g, 40 min, 4 °C) and incubated
353 with Anti-DYKDDDDK G1 Affinity Resin (GenScript) for 1 h and 30 min at 4 °C in gentle
354 agitation. The resin was then washed with Buffer A (50 mM Tris-HCl pH 7.5, 150 mM NaCl,
355 0.01 % LMNG) and elution was performed by incubating for 45 min at room temperature in gentle
356 agitation with Buffer B (50 mM Tris-HCl pH 7.5, 150 mM NaCl, 0.01 % LMNG, 0.2 mg/mL
357 FLAG peptide). The eluate was then concentrated and further purified by size-exclusion
358 chromatography in Buffer C (50 mM Tris-HCl pH 7.5, 150 mM NaCl, 0.0035 % LMNG) on a
359 Superose 6 Increase 10/300 GL (GE Healthcare). For the Ca^{2+} free samples, 2 mM EGTA was also
360 included in Buffer C and for the samples requiring $PI(4,5)P_2$, 50 µM Brain $PI(4,5)P_2$ (L-α-
361 phosphatidylinositol-4,5-bisphosphate (Brain, Porcine) (ammonium salt), Avanti) was added to
362 the buffer B during the elution step and further used to supplement the concentrated eluate before
363 size-exclusion chromatography.

364

365

366 **Cryo-EM sample preparation and data acquisition**

367 hTRPM4 and mTRPM4 samples were concentrated to ~7-8 mg/mL and supplemented with 0.3
368 mM Necrocide 1 ((S')-3-cycloheptyl-3-(4-hydroxyphenyl)-6-methoxy-7-methyl-1,3-
369 dihydroindole-2-one) (NC1). 1 mM EGTA was also added when required. Supplemented samples
370 were incubated for 1 h on ice before vitrification. 4 µL was then applied to a glow-discharged
371 Quantifoil R1.2/1.3 300-mesh gold holey carbon grid (Quantifoil, Micro Tools GmbH, Germany),
372 blotted for 3.5 s under 100 % humidity at 12 °C and plunged into liquid ethane using a Mark IV
373 Vitrobot (FEI).

374 All data collections were performed using SerialEM with a nominal defocus range set from -0.9
375 to -2.2 µm and each movie was recorded with a total dose of 60 $e^-/Å^2$.

376 For the dataset of hTRPM4 containing NC1 and EGTA, movies were acquired on a Titan Krios
377 microscope (FEI) operated at 300 kV with a Falcon4i direct electron detector camera (Thermo
378 Fisher Scientific) at 0.738 Å pixel size.

379 For the dataset of hTRPM4 containing NC1 and PI(4,5)P_2, movies were acquired on a Titan Krios
380 microscope (FEI) operated at 300 kV with a K3 direct electron detector camera (Gatan) using the
381 CDS (Correlated Double Sampling) mode with a super-resolution pixel size of 0.4172 Å.

382 For the datasets of hTRPM4 containing NC1, PI(4,5)P_2 and EGTA and mTRPM4 wild-type
383 containing NC1 and PI(4,5)P_2, movies were acquired on a Titan Krios microscope (FEI) operated
384 at 300 kV with a K3 direct electron detector camera (Gatan) using the CDS (Correlated Double
385 Sampling) mode with a super-resolution pixel size of 0.4285 Å.

386 For the datasets of mTRPM4 wild-type containing NC1 and mTRPM4 L900V/R993P/S1060R
387 triple mutant containing NC1 and PI(4,5)P_2, movies were acquired on a Titan Krios microscope
388 (FEI) operated at 300 kV with a Falcon4i direct electron detector camera (Thermo Fisher Scientific)
389 at 0.735 Å pixel size.

390 **Cryo-EM data processing**

391 The workflow for data processing is summarized in Supplementary Figure 1 and Supplementary
392 Figure 9. Data processing was performed using cryoSPARC (versions 4.3.1 or 4.4.1)[54] following
393 the general scheme described below with some modifications between the datasets. For the dataset

394 of hTRPM4 containing NC1 and PI(4,5)P_2, RELION (version 3.1)[55,56] was also employed in the
395 processing workflow.

396 For the dataset of hTRPM4 containing NC1 and PI(4,5)P_2, movies were motion-corrected and
397 dose-weighted using MotionCor2[57] and CTF estimation was performed using GCTF[58].
398 Micrographs were manually inspected to remove those with bad defocus values and ice
399 contamination. Particles were then picked using Laplacian-of-Gaussian (LoG) and extracted in
400 RELION. Extracted particles were subjected to multiple rounds of 2D classification and classes
401 displaying clear features of the TRPM4 channel were used for subsequent 3D classification. The
402 particles from the best-resolving 3D classes along with the respective 3D volumes were then
403 imported into cryoSPARC and used for 3D heterogeneous refinement and 3D classification
404 without alignment to remove junk particles and differentiate channel conformations. The best-
405 resolving 3D classes were refined using Non-Uniform refinement with imposed C4 symmetry[59].

406 For all other datasets, movies were subjected to patch motion correction and subsequent patch CTF
407 estimation in cryoSPARC. The resulting micrographs were manually curated and those exhibiting
408 drift, poor CTF estimation and outliers in defocus values and ice thickness were excluded from
409 further processing (individually assessed for each parameter relative to the overall distribution).
410 An initial round of particle picking was carried out with blob picker. Particles were then extracted
411 and subjected to one round of 2D classification. Classes displaying clear features of the TRPM4
412 channel were selected and used either directly for subsequent processing or to re-pick particles
413 with template picker. Additional rounds of 2D classification were further performed and particles
414 from selected classes were used to obtain an initial 3D reconstruction with Ab-Initio. 3D
415 heterogeneous refinement was then employed to remove junk particles, and the resulting particles
416 were subjected to 3D classification without alignment to differentiate channel conformations. The
417 best-resolving 3D classes were refined using Non-Uniform refinement with imposed C4
418 symmetry[59].

419 Map resolutions were reported according to the gold-standard Fourier shell correlation (FSC) using
420 the 0.143 criterion[60]. Local resolutions and angular distributions were estimated in cryoSPARC.

421

422

423 **Model building**

424 Initial models were obtained using a combination of ModelAngelo[61] and previously available
425 hTRPM4 (PDBs: 9MTA and 9MRT) and mTRPM4 (PDB:6BCJ) structures. The models were then
426 manually adjusted in Coot[62] and refined against the respective maps in PHENIX[63]. Ligand
427 restraints CIF files were generated using the Grade2 Web Server[64]. The geometry statistics of the
428 models were obtained using MolProbity[65]. All the structural figures were prepared using UCSF
429 ChimeraX[66,67].

430 **Electrophysiology**

431 Wild-type human and mouse TRPM4, along with the respective mutants, were cloned into a
432 pEGFP-N1 plasmid (Clontech). Mutants were generated by site-directed mutagenesis using the
433 QuickChange method and verified by sequencing. 1 µg of plasmid was transfected into HEK293
434 cells using Lipofectamine 2000 (Life Technology). 48 h after transfection, cells were dissociated
435 by trypsin treatment and kept in a complete serum-containing medium before being re-plated onto
436 35-mm tissue culture dishes and incubated in a tissue culture incubator until recording.

437 Channel currents were recorded in whole cell or excised inside-out configuration. The long-chain
438 native Brain PI(4,5)P_2 employed in the structural studies is insoluble in water and forms liposomes
439 in the recording solutions, making it difficult to fuse into the patch membrane. Therefore, the
440 water-soluble short-chain synthetic PI(4,5)P_2 diC8 (Phosphatidylinositol 4,5-bisphosphate diC8,
441 Echelon Bioscience) was used in the functional experiments as needed. For inside-out patches, the
442 standard bath solution (cytosolic side) contained (in mM): 145 caesium methanesulfonate (Cs–
443 MS), 5 NaCl, 1 $MgCl_2$, 0.3 $CaCl_2$, 10 HEPES buffered with Tris, pH 7.4. 10 µM NC1 and/or 10
444 µM PI(4,5)P_2 diC8 were added to the bath solution when required. For the calcium-free condition,
445 0.5 mM EGTA was added to the bath solution without $CaCl_2$. The pipette solution (extracellular
446 side) contained (in mM): 140 Na–MS, 1 $MgCl_2$, 5 $CaCl_2$, 10 HEPES buffered with Tris, pH 7.4.
447 For whole cell current recordings, the pipette solution contained (in mM): Cs-MS 140, CsCl 4,
448 $MgCl_2$ 1, EGTA 1 or 10, HEPES 10, buffered with Tris, pH 7.4. Bath solution contained (in mM):
449 Na-MS 140, NaCl 5, $MgCl_2$ 1, $CaCl_2$ 1, HEPES 10, buffered with Tris, pH=7.4. 10 µM NC1 was
450 added to the bath solution as needed. Patch pipettes were pulled from borosilicate glass (Harvard
451 Apparatus) and heat polished to a resistance of 3–5 MΩ. After the patch pipette was attached to

452 the cell membrane, a giga seal (> 10 GΩ) was formed by gentle suction. The inside-out
453 configuration was formed by pulling the pipette away from the cell and the pipette tip was exposed
454 to air for a short time in some cases. The holding potential was set to 0 mV. The current and voltage
455 relationship (I–V curve) was obtained using voltage pulses ramped from – 100 to + 100 mV over
456 an 800 ms duration every 2 seconds. Data was acquired using an AxoPatch 200B amplifier
457 (Molecular Devices) and a low-pass analog filter set to 1 kHz. The current signal was sampled at
458 a rate of 20 kHz using a Digidata 1322A digitizer (Molecular Devices) and further analyzed with
459 pClamp 11 software (Molecular Devices). Sample traces for the I–V curves of macroscopic
460 currents shown were obtained from recordings on the same patch. Bars represent mean ± SEM of
461 five measurements from different patches (n = 5 independent biological replicates).

462 **Cell death assay**

463 Cell death was assessed in HeLa cells transiently expressing EGFP-tagged human or mouse
464 TRPM4 by monitoring the morphological change of transfected cells using microscopy, as
465 described previously[40]. Briefly, HeLa cells were seeded onto glass coverslips and grown to 30–
466 40% confluency before transfection. 24 hours after TRPM4-EGFP transfection, cells were
467 subjected to 1 μM NC1 treatment. Fluorescence images were taken before and after the indicated
468 period of treatment. The morphological changes of cells with green fluorescence were monitored
469 using microscopy, and over 50 cells expressing TRPM4 were analyzed in each group.

470 **Cell viability assay**

471 Cell viability was assessed in HeLa cells stably expressing human or mouse TRPM4, using the
472 CellTiter-Glo (CTG) assay as described previously[40]. Briefly, cells were seeded in a 96-well plate
473 at a density of $1x10^4$ cells per well and allowed to adhere overnight. After treatment with various
474 experimental conditions, the intracellular ATP was measured using the CTG luminescent assay kit
475 (Promega, G7570) according to the manufacturer's instructions. Briefly, 100 μL of CTG reagent
476 was added to each well, and the plate was gently shaken for 10 minutes to induce cell lysis and
477 release of intracellular ATP. The luminescence signal, proportional to the amount of ATP present
478 and indicative of cell viability, was measured using a multi-well plate reader. All experiments were
479 repeated three times, and the results were presented as mean ± SD.

480

481 **Cell surface biotinylation assay and western blot**

482 Surface protein biotinylation was employed to assess the expression levels of wild-type hTRPM4
483 and respective PI(4,5)P_2 binding site mutants used in the electrophysiology experiments. The assay
484 was performed using the Cell Surface Biotinylation and Isolation Kit (Pierce, A44390) according
485 to the manufacturer's instructions. Briefly, transfected HEK293 cells were washed with PBS and
486 incubated with Sulfo-NHS-SS-Biotin labeling solution for 30 min at 4 °C. The cells were then
487 washed three times with ice-cold TBS to quench and remove the non-reacted biotinylation reagent,
488 scraped, and collected by centrifugation (500 g, 3 min). Cell lysis was carried out using the
489 supplied lysis buffer supplemented with protease inhibitors, and clarified lysates were collected
490 by centrifugation (15000 g, 5 min, 4°C) and incubated with NeutrAvidin Agarose beads for 30
491 min at room temperature using gentle rotation. After washing, the bound biotinylated surface
492 proteins were eluted by incubating the beads with the supplied elution buffer supplemented with
493 10 mM DTT for 30 min at room temperature using gentle rotation. Clarified lysates and eluted
494 proteins were separated by SDS-PAGE and transferred to PVDF membranes for immunoblotting.
495 hTRPM4 was probed using the anti-GFP-tag rabbit monoclonal antibody (Thermo Fisher
496 Scientific, G10362). The surface protein CD44 was used as a loading control and probed with the
497 Anti-CD44 rabbit polyclonal antibody (Abcam, ab157107).

498

499 ## Data availability

500 The cryo-EM density maps of the human TRPM4 have been deposited in the Electron Microscopy
501 Data Bank (EMDB) under accession numbers EMD-73526 (NC1-bound in the presence of EGTA),
502 EMD-73527 (NC1/PI(4,5)P_2-bound), and EMD-73528 (NC1/PI(4,5)P_2-bound in the presence of
503 EGTA). Atomic coordinates have been deposited in the Protein Data Bank (PDB) under accession
504 numbers 9YVK (NC1-bound in the presence of EGTA), 9YVL (NC1/PI(4,5)P_2-bound), and
505 9YVM (NC1/PI(4,5)P_2-bound in the presence of EGTA).

506 The cryo-EM density maps of the mouse TRPM4 have been deposited in the Electron Microscopy
507 Data Bank (EMDB) under accession numbers EMD-73530 (NC1/PI(4,5)P_2-bound wild-type
508 mTRPM4), EMD-73529 (NC1-bound wild-type mTRPM4), and EMD-73531 (NC1/PI(4,5)P_2-
509 bound L900V/R993P/S1060R triple mutant mTRPM4). Atomic coordinates have been deposited

510 in the Protein Data Bank (PDB) under accession numbers 9YVO (NC1/PI(4,5)P_2-bound wild-type
511 mTRPM4), 9YVN (NC1-bound wild-type mTRPM4), and 9YVP (NC1/PI(4,5)P_2-bound
512 L900V/R993P/S1060R triple mutant mTRPM4).

513 All other data and materials supporting the findings of this study can be obtained from the
514 corresponding authors upon reasonable request.

515 # References

516 1 Launay, P. *et al.* TRPM4 is a Ca2+-activated nonselective cation channel mediating cell
517 membrane depolarization. *Cell* **109**, 397-407 (2002). https://doi.org/10.1016/s0092-
518 8674(02)00719-5
519 2 Montell, C. *et al.* A Unified Nomenclature for the Superfamily of TRP Cation Channels. *Molecular*
520 *Cell* **9**, 229-231 (2002). https://doi.org/https://doi.org/10.1016/S1097-2765(02)00448-3
521 3 Nilius, B. *et al.* Voltage dependence of the Ca2+-activated cation channel TRPM4. *J Biol Chem*
522 **278**, 30813-30820 (2003). https://doi.org/10.1074/jbc.M305127200
523 4 Fonfria, E. *et al.* Tissue Distribution Profiles of the Human TRPM Cation Channel Family. *Journal*
524 *of Receptors and Signal Transduction* **26**, 159-178 (2006).
525 https://doi.org/10.1080/10799890600637506
526 5 Demion, M., Bois, P., Launay, P. & Guinamard, R. TRPM4, a Ca2+-activated nonselective cation
527 channel in mouse sino-atrial node cells. *Cardiovasc Res* **73**, 531-538 (2007).
528 https://doi.org/10.1016/j.cardiores.2006.11.023
529 6 Guinamard, R., Demion, M., Chatelier, A. & Bois, P. Calcium-Activated Nonselective Cation
530 Channels in Mammalian Cardiomyocytes. *Trends in Cardiovascular Medicine* **16**, 245-250 (2006).
531 https://doi.org/https://doi.org/10.1016/j.tcm.2006.04.007
532 7 Hof, T. *et al.* TRPM4 non-selective cation channel variants in long QT syndrome. *BMC Med Genet*
533 **18**, 31 (2017). https://doi.org/10.1186/s12881-017-0397-4
534 8 Stallmeyer, B. *et al.* Mutational spectrum in the Ca2+-activated cation channel gene TRPM4 in
535 patients with cardiac conductance disturbances. *Human Mutation* **33**, 109-117 (2012).
536 https://doi.org/https://doi.org/10.1002/humu.21599
537 9 Launay, P. *et al.* TRPM4 regulates calcium oscillations after T cell activation. *Science* **306**, 1374-
538 1377 (2004). https://doi.org/10.1126/science.1098845
539 10 Becerra, A. *et al.* Transient receptor potential melastatin 4 inhibition prevents
540 lipopolysaccharide-induced endothelial cell death. *Cardiovascular Research* **91**, 677-684 (2011).
541 https://doi.org/10.1093/cvr/cvr135
542 11 Gerzanich, V. *et al.* De novo expression of Trpm4 initiates secondary hemorrhage in spinal cord
543 injury. *Nature Medicine* **15**, 185-191 (2009). https://doi.org/10.1038/nm.1899
544 12 Ghosh, S. *et al.* Plasma Membrane Channel TRPM4 Mediates Immunogenic Therapy-Induced
545 Necrosis. *Cancer Res* **83**, 3115-3130 (2023). https://doi.org/10.1158/0008-5472.Can-23-0157
546 13 Schattling, B. *et al.* TRPM4 cation channel mediates axonal and neuronal degeneration in
547 experimental autoimmune encephalomyelitis and multiple sclerosis. *Nature Medicine* **18**, 1805-
548 1811 (2012). https://doi.org/10.1038/nm.3015
549 14 Simon, F. *et al.* Hydrogen peroxide removes TRPM4 current desensitization conferring increased
550 vulnerability to necrotic cell death. *J Biol Chem* **285**, 37150-37158 (2010).
551 https://doi.org/10.1074/jbc.M110.155390
552 15 Borgström, A., Peinelt, C. & Stokłosa, P. TRPM4 in Cancer-A New Potential Drug Target.
553 *Biomolecules* **11** (2021). https://doi.org/10.3390/biom11020229
554 16 Berg, K. D. *et al.* TRPM4 protein expression in prostate cancer: a novel tissue biomarker
555 associated with risk of biochemical recurrence following radical prostatectomy. *Virchows Archiv*
556 **468**, 345-355 (2016). https://doi.org/10.1007/s00428-015-1880-y
557 17 Holzmann, C. *et al.* Transient receptor potential melastatin 4 channel contributes to migration of
558 androgen-insensitive prostate cancer cells. *Oncotarget* **6** (2015).
559 18 Sagredo, A. I. *et al.* TRPM4 channel is involved in regulating epithelial to mesenchymal
560 transition, migration, and invasion of prostate cancer cell lines. *Journal of Cellular Physiology*
561 **234**, 2037-2050 (2019). https://doi.org/https://doi.org/10.1002/jcp.27371

562 19 Guo, J. *et al.* TRPM4 channels contribute to Adriamycin chemoresistance in breast cancer cells.
563 *European Journal of Pharmacology* **998**, 177637 (2025).
564 https://doi.org/https://doi.org/10.1016/j.ejphar.2025.177637
565 20 Wong, K. K. & Hussain, F. A. TRPM4 is overexpressed in breast cancer associated with estrogen
566 response and epithelial-mesenchymal transition gene sets. *PLOS ONE* **15**, e0233884 (2020).
567 https://doi.org/10.1371/journal.pone.0233884
568 21 Loo, S. K. *et al.* TRPM4 expression is associated with activated B cell subtype and poor survival in
569 diffuse large B cell lymphoma. *Histopathology* **71**, 98-111 (2017).
570 https://doi.org/10.1111/his.13204
571 22 Wang, F. *et al.* Aberrant TRPM4 expression in MLL-rearranged acute myeloid leukemia and its
572 blockade induces cell cycle arrest via AKT/GLI1/Cyclin D1 pathway. *Cellular Signalling* **72**, 109643
573 (2020). https://doi.org/https://doi.org/10.1016/j.cellsig.2020.109643
574 23 Amarouch, M.-Y., Syam, N. & Abriel, H. Biochemical, single-channel, whole-cell patch clamp, and
575 pharmacological analyses of endogenous TRPM4 channels in HEK293 cells. *Neuroscience Letters*
576 **541**, 105-110 (2013). https://doi.org/https://doi.org/10.1016/j.neulet.2013.02.011
577 24 Burris, S. K., Wang, Q., Bulley, S., Neeb, Z. P. & Jaggar, J. H. 9-Phenanthrol inhibits recombinant
578 and arterial myocyte TMEM16A channels. *Br J Pharmacol* **172**, 2459-2468 (2015).
579 https://doi.org/10.1111/bph.13077
580 25 Gardam, K. E., Geiger, J. E., Hickey, C. M., Hung, A. Y. & Magoski, N. S. Flufenamic acid affects
581 multiple currents and causes intracellular Ca2+ release in Aplysia bag cell neurons. *J*
582 *Neurophysiol* **100**, 38-49 (2008). https://doi.org/10.1152/jn.90265.2008
583 26 Guinamard, R. *et al.* Functional characterization of a Ca2+-activated non-selective cation channel
584 in human atrial cardiomyocytes. *The Journal of Physiology* **558**, 75-83 (2004).
585 https://doi.org/https://doi.org/10.1113/jphysiol.2004.063974
586 27 Hu, J. *et al.* Physiological temperature drives TRPM4 ligand recognition and gating. *Nature* **630**,
587 509-515 (2024). https://doi.org/10.1038/s41586-024-07436-7
588 28 Chen, B. *et al.* TRPM4-specific blocking antibody attenuates reperfusion injury in a rat model of
589 stroke. *Pflugers Arch* **471**, 1455-1466 (2019). https://doi.org/10.1007/s00424-019-02326-8
590 29 Low, S. W. *et al.* Development and characterization of a monoclonal antibody blocking human
591 TRPM4 channel. *Sci Rep* **11**, 10411 (2021). https://doi.org/10.1038/s41598-021-89935-5
592 30 Wei, S. *et al.* Binding epitope for recognition of human TRPM4 channel by monoclonal antibody
593 M4M. *Scientific Reports* **12**, 19562 (2022). https://doi.org/10.1038/s41598-022-22077-4
594 31 Wei, S. *et al.* Development and in vitro characterization of humanized antibodies for blocking
595 human TRPM4 channel. *Sci Rep* **15**, 19769 (2025). https://doi.org/10.1038/s41598-025-05256-x
596 32 Ozhathil, L. C. *et al.* Identification of potent and selective small molecule inhibitors of the cation
597 channel TRPM4. *Br J Pharmacol* **175**, 2504-2519 (2018). https://doi.org/10.1111/bph.14220
598 33 Binkle-Ladisch, L. *et al.* Identification and development of TRPM4 antagonists to counteract
599 neuronal excitotoxicity. *iScience* **27**, 111425 (2024). https://doi.org/10.1016/j.isci.2024.111425
600 34 Arullampalam, P. *et al.* Species-Specific Effects of Cation Channel TRPM4 Small-Molecule
601 Inhibitors. *Front Pharmacol* **12**, 712354 (2021). https://doi.org/10.3389/fphar.2021.712354
602 35 Ekundayo, B. *et al.* Identification of a binding site for small molecule inhibitors targeting human
603 TRPM4. *Nat Commun* **16**, 833 (2025). https://doi.org/10.1038/s41467-025-56131-2
604 36 Teixeira-Duarte, C. M., Zeng, W. & Jiang, Y. Structural landscape of activation, desensitization
605 and inhibition in the human TRPM4 channel. *Nature Structural & Molecular Biology* (2025).
606 https://doi.org/10.1038/s41594-025-01705-3
607 37 Christensen, M. K. *et al.* Synthesis and antitumor effect in vitro and in vivo of substituted 1,3-
608 dihydroindole-2-ones. *J Med Chem* **53**, 7140-7145 (2010). https://doi.org/10.1021/jm100763j

38 Trojel-Hansen, C. *et al.* Novel small molecule drugs inhibit tumor cell metabolism and show potent anti-tumorigenic potential. *Cancer Chemother Pharmacol* **68**, 127-138 (2011). https://doi.org/10.1007/s00280-010-1453-3

39 Zhang, J. *et al.* Necrocide 1 mediates necrotic cell death and immunogenic response in human cancer cells. *Cell Death Dis* **14**, 238 (2023). https://doi.org/10.1038/s41419-023-05740-0

40 Fu, W. *et al.* Persistent activation of TRPM4 triggers necrotic cell death characterized by sodium overload. *Nature Chemical Biology* (2025). https://doi.org/10.1038/s41589-025-01841-3

41 Qiao, Y. *et al.* Sodium disrupts mitochondrial energy metabolism to execute NECSO. *Nature Communications* **17**, 493 (2025). https://doi.org/10.1038/s41467-025-67181-x

42 Fulda, S. & Debatin, K. M. Extrinsic versus intrinsic apoptosis pathways in anticancer chemotherapy. *Oncogene* **25**, 4798-4811 (2006). https://doi.org/10.1038/sj.onc.1209608

43 Singh, R., Letai, A. & Sarosiek, K. Regulation of apoptosis in health and disease: the balancing act of BCL-2 family proteins. *Nature Reviews Molecular Cell Biology* **20**, 175-193 (2019). https://doi.org/10.1038/s41580-018-0089-8

44 Nilius, B. *et al.* The Ca2+-activated cation channel TRPM4 is regulated by phosphatidylinositol 4,5-biphosphate. *Embo j* **25**, 467-478 (2006). https://doi.org/10.1038/sj.emboj.7600963

45 Zhang, Z., Okawa, H., Wang, Y. & Liman, E. R. Phosphatidylinositol 4,5-bisphosphate rescues TRPM4 channels from desensitization. *J Biol Chem* **280**, 39185-39192 (2005). https://doi.org/10.1074/jbc.M506965200

46 Ong, S. T., Tyagi, A., Chandy, K. G. & Bhushan, S. Mechanisms Underlying C-type Inactivation in Kv Channels: Lessons From Structures of Human Kv1.3 and Fly Shaker-IR Channels. *Frontiers in Pharmacology* **Volume 13 - 2022** (2022). https://doi.org/10.3389/fphar.2022.924289

47 Liu, Y. *et al.* Noncanonical calcium-independent TRPM4 activation governs intestinal fluid homeostasis. *Nature Communications* **17**, 1253 (2026). https://doi.org/10.1038/s41467-025-68014-7

48 Yin, Y. *et al.* Molecular basis of neurosteroid and anticonvulsant regulation of TRPM3. *Nature Structural & Molecular Biology* **32**, 828-840 (2025). https://doi.org/10.1038/s41594-024-01463-8

49 Kumar, S. *et al.* Structural basis for agonist and heat activation of nociceptor TRPM3. *Nature Structural & Molecular Biology* (2025). https://doi.org/10.1038/s41594-025-01692-5

50 Yin, Y. *et al.* Structural basis of cooling agent and lipid sensing by the cold-activated TRPM8 channel. *Science* **363**, eaav9334 (2019). https://doi.org/doi:10.1126/science.aav9334

51 Yin, Y. *et al.* Mechanisms of sensory adaptation and inhibition of the cold and menthol receptor TRPM8. *Science Advances* **10**, eadp2211 (2024). https://doi.org/doi:10.1126/sciadv.adp2211

52 Zhao, C. *et al.* Structures of a mammalian TRPM8 in closed state. *Nature Communications* **13**, 3113 (2022). https://doi.org/10.1038/s41467-022-30919-y

53 Morales-Perez, C. L., Noviello, C. M. & Hibbs, R. E. Manipulation of Subunit Stoichiometry in Heteromeric Membrane Proteins. *Structure* **24**, 797-805 (2016). https://doi.org/10.1016/j.str.2016.03.004

54 Punjani, A., Rubinstein, J. L., Fleet, D. J. & Brubaker, M. A. cryoSPARC: algorithms for rapid unsupervised cryo-EM structure determination. *Nature Methods* **14**, 290-296 (2017). https://doi.org/10.1038/nmeth.4169

55 Scheres, S. H. W. RELION: Implementation of a Bayesian approach to cryo-EM structure determination. *Journal of Structural Biology* **180**, 519-530 (2012). https://doi.org/https://doi.org/10.1016/j.jsb.2012.09.006

56 Zivanov, J. *et al.* New tools for automated high-resolution cryo-EM structure determination in RELION-3. *Elife* **7** (2018). https://doi.org/10.7554/eLife.42166

656 57 Zheng, S. Q. *et al.* MotionCor2: anisotropic correction of beam-induced motion for improved
657 cryo-electron microscopy. *Nature Methods* **14**, 331-332 (2017).
658 https://doi.org/10.1038/nmeth.4193
659 58 Zhang, K. Gctf: Real-time CTF determination and correction. *Journal of Structural Biology* **193**, 1-
660 12 (2016). https://doi.org/https://doi.org/10.1016/j.jsb.2015.11.003
661 59 Punjani, A., Zhang, H. & Fleet, D. J. Non-uniform refinement: adaptive regularization improves
662 single-particle cryo-EM reconstruction. *Nature Methods* **17**, 1214-1221 (2020).
663 https://doi.org/10.1038/s41592-020-00990-8
664 60 Henderson, R. *et al.* Outcome of the first electron microscopy validation task force meeting.
665 *Structure* **20**, 205-214 (2012). https://doi.org/10.1016/j.str.2011.12.014
666 61 Jamali, K. *et al.* Automated model building and protein identification in cryo-EM maps. *Nature*
667 **628**, 450-457 (2024). https://doi.org/10.1038/s41586-024-07215-4
668 62 Emsley, P., Lohkamp, B., Scott, W. G. & Cowtan, K. Features and development of Coot. *Acta*
669 *Crystallographica Section D* **66**, 486-501 (2010).
670 https://doi.org/doi:10.1107/S0907444910007493
671 63 Liebschner, D. *et al.* Macromolecular structure determination using X-rays, neutrons and
672 electrons: recent developments in Phenix. *Acta Crystallographica Section D* **75**, 861-877 (2019).
673 https://doi.org/doi:10.1107/S2059798319011471
674 64 Smart, O. S., Sharff A., Holstein, J., Womack, T.O., Flensburg, C., Keller, P., Paciorek, W.,
675 Vonrhein, C. and Bricogne G. Grade2 version 1.6.0. *Cambridge, United Kingdom:Global Phasing*
676 *Ltd.* (2021).
677 65 Chen, V. B. *et al.* MolProbity: all-atom structure validation for macromolecular crystallography.
678 *Acta Crystallogr D Biol Crystallogr* **66**, 12-21 (2010).
679 https://doi.org/10.1107/s0907444909042073
680 66 Pettersen, E. F. *et al.* UCSF ChimeraX: Structure visualization for researchers, educators, and
681 developers. *Protein Sci* **30**, 70-82 (2021). https://doi.org/10.1002/pro.3943
682 67 Meng, E. C. *et al.* UCSF ChimeraX: Tools for structure building and analysis. *Protein Science* **32**,
683 e4792 (2023). https://doi.org/https://doi.org/10.1002/pro.4792

684

685

Acknowledgements

Single particle cryo-EM data were collected at the University of Texas Southwestern Medical Center Cryo-EM Facility (CEMF) funded by the CPRIT Core Facility Support Award RP170644 and at Howard Hughes Medical Institute Janelia Cryo-EM Facility. Cryo-EM sample grids were prepared at the Structural Biology Laboratory at UT Southwestern Medical Center partially supported by grant RP170644 from CPRIT. This work was supported in part by the Howard Hughes Medical Institute (to Y.J.) and by grant from the National Institute of Health (R35GM140892 to Y.J.), and by grants from MOST (Ministry of Science and Technology of the People's Republic of China) (2023YFA0914900 to Q.Z.), NSFC (National Natural Science Foundation of China) (W2511018, 32530055 to Q.Z., 82504119 to W.F.). This article is subject to HHMI's Open Access to Publications policy. HHMI lab heads have previously granted a nonexclusive CC BY 4.0 license to the public and a sublicensable license to HHMI in their research articles. Pursuant to those licenses, the author-accepted manuscript of this article can be made freely available under a CC BY 4.0 license immediately upon publication.

Author Contributions

C.T-D. prepared the purified protein samples, performed data acquisition, image processing, and structure determination; W.F. established the cell death assay system, led the functional characterization, and identified the key residues underlying the species-specific response of TRPM4 to NC1; W.Z. performed electrophysiology recording; J.W., X.J., and Z.Z assisted with mutagenesis and cell death assay; Y.J. and Q.Z. supervised the work. All authors participated in research design, data analysis, discussion, and manuscript preparation.

Competing interests

The authors declare no competing interests.

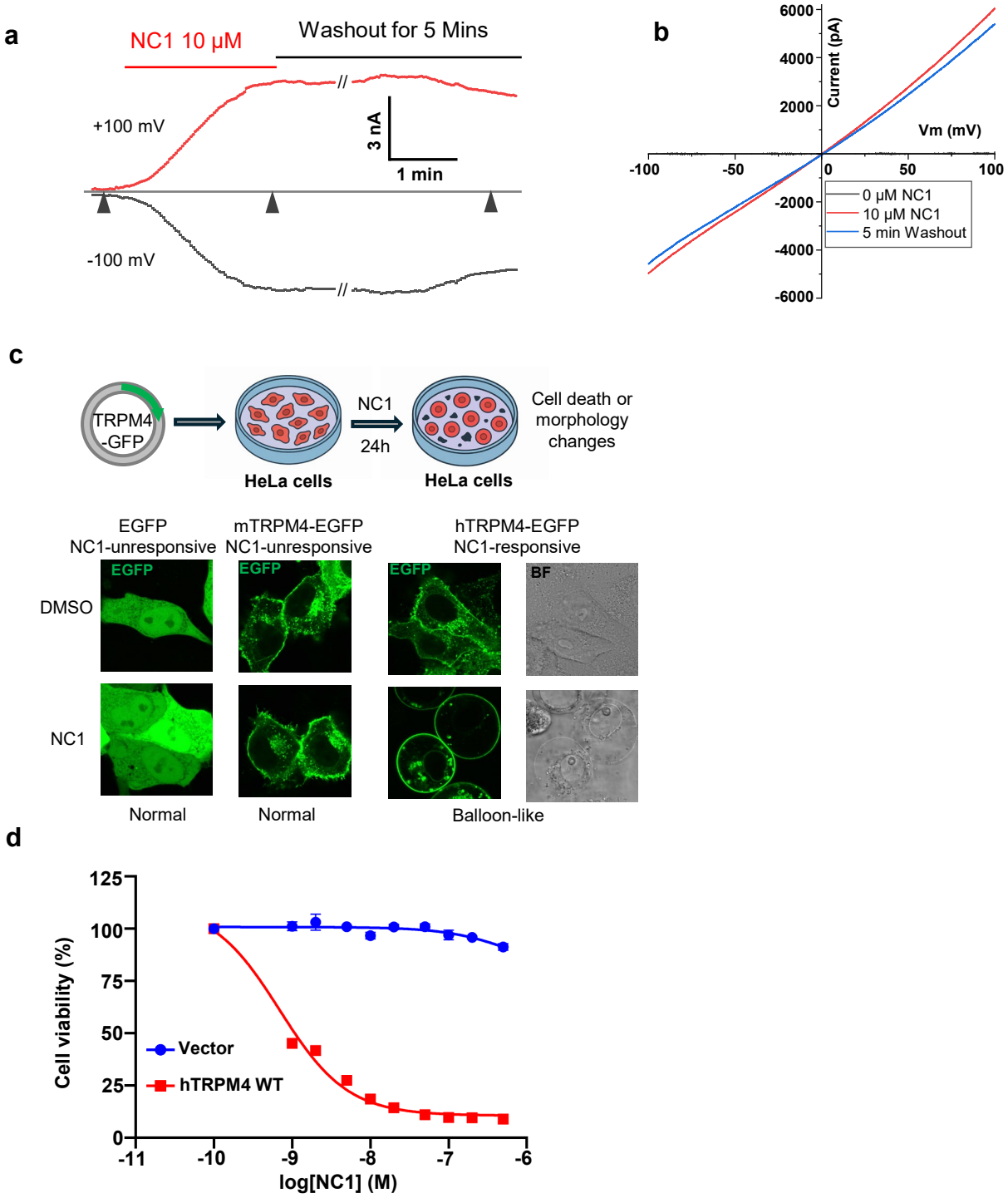

Fig. 1: NC1 activation of hTRPM4. a Macroscopic currents of hTRPM4 overexpressed in HEK293 cells at ±100 mV in a whole-cell patch with the presence or absence of 10 μM NC1 in the bath (extracellular). Triangles mark the time points of three NC1-mediated hTRPM4 activation states (left to right): Closed channel in the absence of NC1; Fully activated channel 2 min after NC1 addition; Channel current retained 5 min after NC1 washout. **b** Sample I-V curves measured at the time points marked by the triangles shown in **a**. **c** NC1-induced cell death assay. Top panel: schematic illustration of the assay. Bottom panels: morphologies of EGFP, EGFP-tagged mTRPM4, or EGFP-tagged hTRPM4-expressing HeLa cells 24 hours after DMSO (NC1 solvent) or NC1 (1 μM) treatment. **d** Dose-dependent NC1 cytotoxicity in HeLa cells stably expressing wild-type hTRPM4. Data points represent mean ± SD of n = 3 independent replicates.

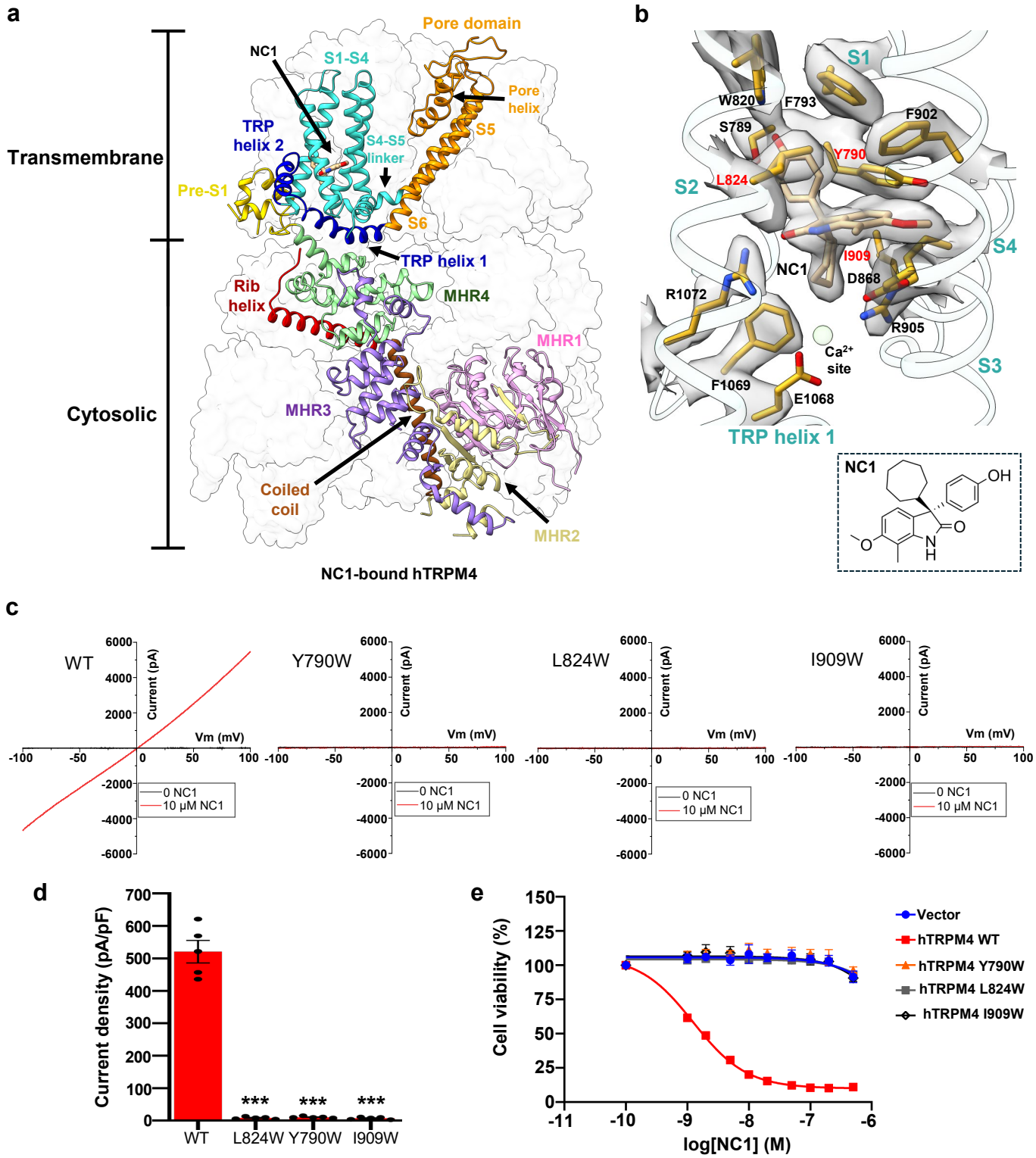

Fig. 2: NC1 binding in hTRPM4. a Structure of NC1-bound hTRPM4. The front subunit is depicted in a cartoon representation, with each domain individually colored. **b** Zoomed-in view of the NC1 binding site. NC1 and its surrounding residues are shown in stick representation. The light green sphere marks the calcium activation site. Density for NC1 and its surrounding residues (grey surface) is contoured at 0.2 in ChimeraX. Residues sensitive to tryptophan substitution are labeled in red. **c** Sample I-V curves of wild-type hTRPM4 and its tryptophan substitutions at the NC1-binding site recorded in whole-cell patches with 10 μM NC1 in the bath (extracellular). **d** Outward current density of NC1-activated wild-type hTRPM4 and its tryptophan mutations recorded at +100 mV in whole-cell patches with 10 μM NC1 in the bath (extracellular). Bars represent mean ± SEM of n=5 independent replicates (shown as dots). p-values were calculated using a two-sided Student's t-test and are provided in the Source Data file. *** represents $p < 0.001$. **e** Dose-dependent NC1 cytotoxicity in HeLa cells stably expressing wild-type hTRPM4 or its tryptophan mutations. Data points represent mean ± SD of n = 3 independent replicates.

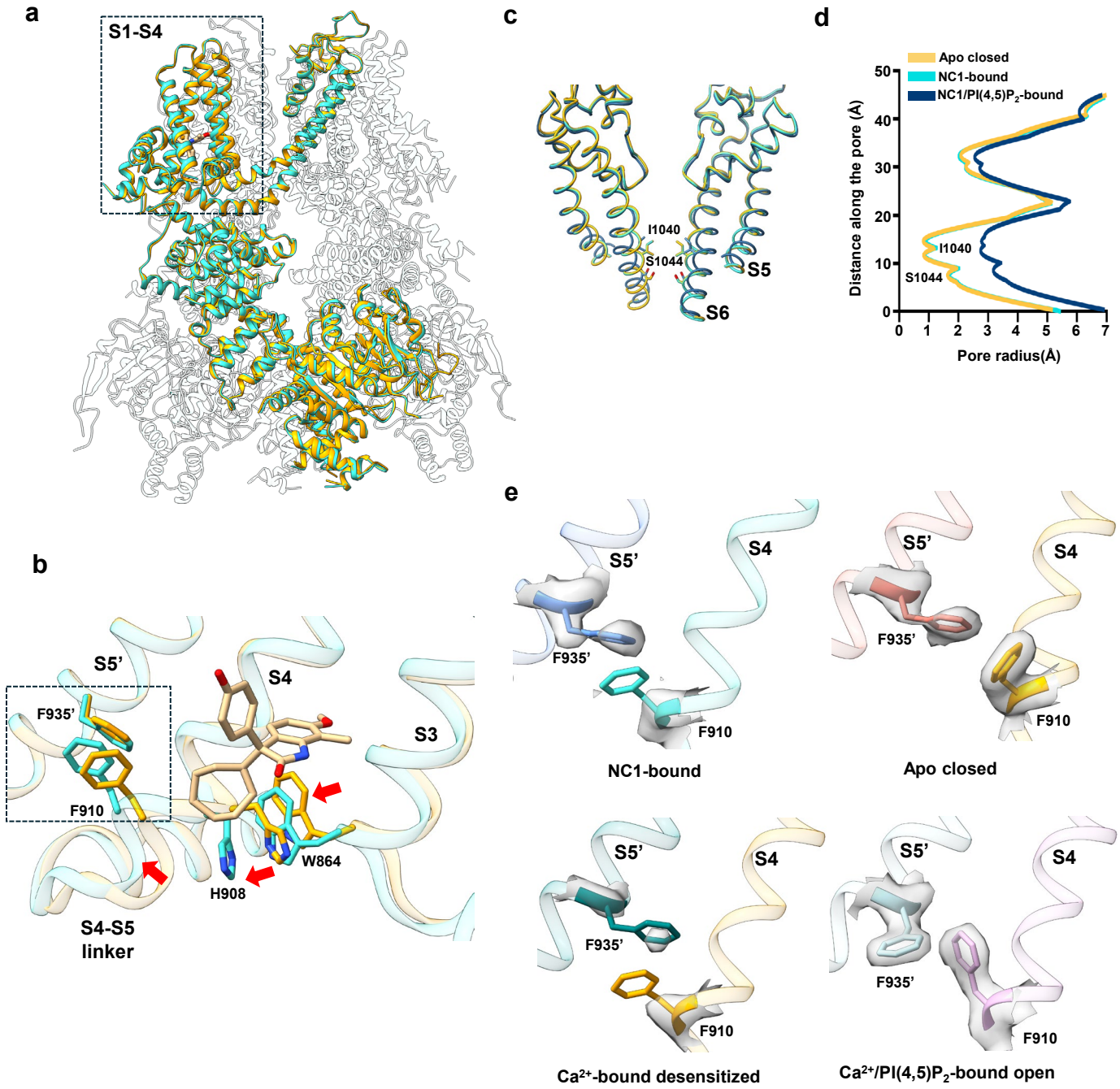

Fig. 3: hTRPM4 conformational changes induced by NC1 binding. a Superposition of the hTRPM4 structures in the NC1-bound and apo closed (PDB:9MTA) states with the front subunits highlighted in cyan and orange, respectively. **b** Local conformational changes at the S1-S4 domain between NC1-bound (cyan) and apo closed (orange) hTRPM4. Only S3-S4 and the neighboring S5 (marked with a single quotation mark) are displayed for clarity. Red arrows mark the major movements upon NC1 binding. Key residues are shown in stick representation. **c** Structural comparison of the hTRPM4 ion conduction pore in the apo closed (orange), NC1-bound (cyan), and NC1/PI(4,5)P_2-bound (navy blue) states. Gating residues I1040 and S1044 are shown in stick representation. The front and back subunits are removed for clarity. **d** Pore radius of hTRPM4 along the central axis in the apo closed, NC1-bound, and NC1/PI(4,5)P_2-bound structures. **e** F935'-F910 contact interface in the NC1-bound, apo closed, Ca^{2+}-bound desensitized (PDB:9MT8), and Ca^{2+}/PI(4,5)P_2-bound open (PDB:9MRT) states. The EM density maps for F910 and F935' are shown in grey surface contoured at 0.23 in ChimeraX.

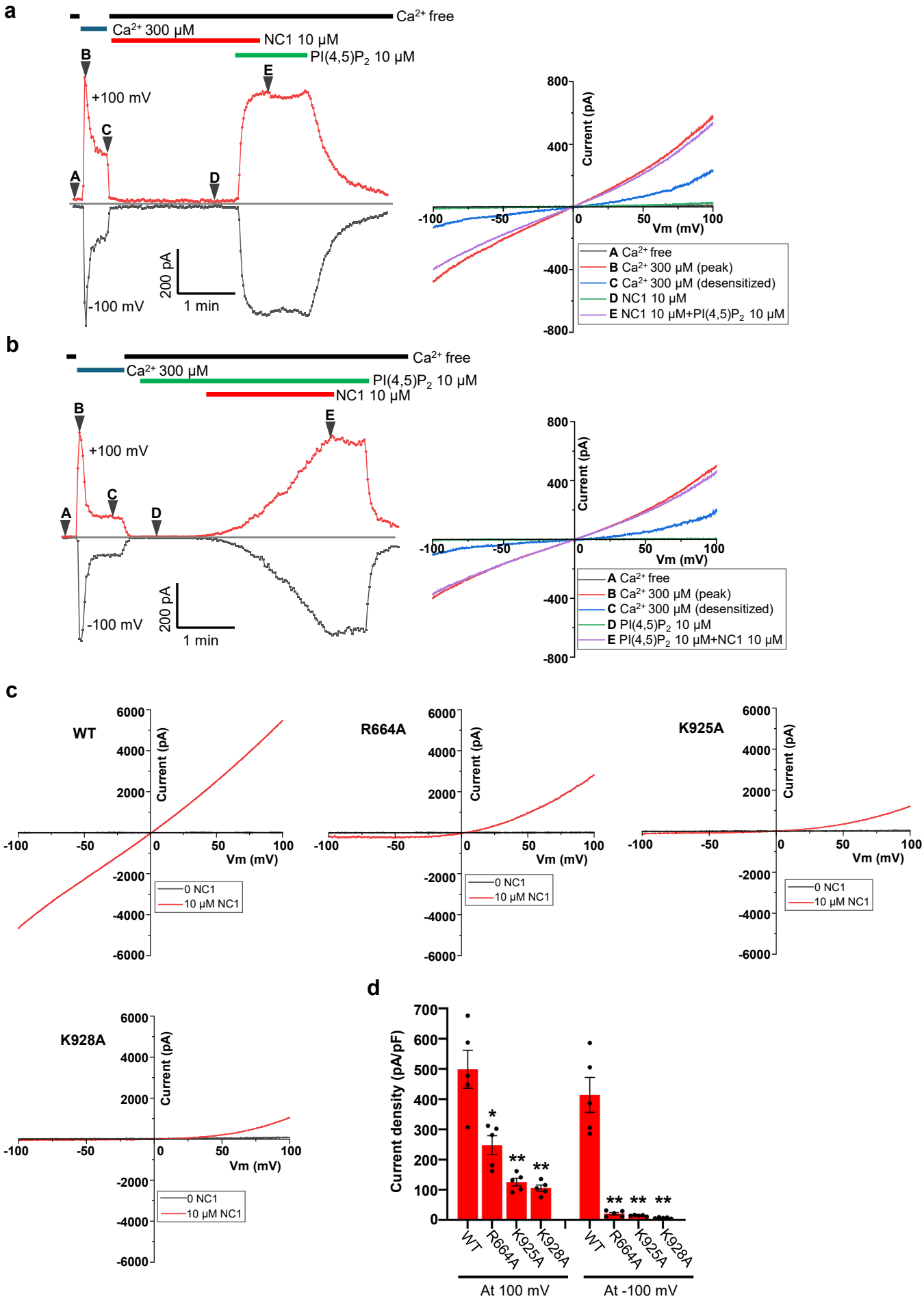
a
Ca2+ free
Ca2+ 300 μM
NC1 10 μM
PI(4,5)P2 10 μM
B
E
+100 mV
C
A
D
-100 mV
200 pA
1 min
Current (pA)
Vm (mV)
A Ca2+ free
B Ca2+ 300 μM (peak)
C Ca2+ 300 μM (desensitized)
D NC1 10 μM
E NC1 10 μM+PI(4,5)P2 10 μM
b
Ca2+ free
Ca2+ 300 μM
PI(4,5)P2 10 μM
NC1 10 μM
B
E
+100 mV
C
A
D
-100 mV
200 pA
1 min
Current (pA)
Vm (mV)
A Ca2+ free
B Ca2+ 300 μM (peak)
C Ca2+ 300 μM (desensitized)
D PI(4,5)P2 10 μM
E PI(4,5)P2 10 μM+NC1 10 μM
c
WT
R664A
K925A
K928A
Current (pA)
Vm (mV)
0 NC1
10 μM NC1
d
Current density (pA/pF)
WT
R664A
K925A
K928A
At 100 mV
At -100 mV

Fig. 4 PI(4,5)P_2-dependent NC1 activation of hTRPM4. a Macroscopic currents of hTRPM4-expressing HEK293 cells at ±100 mV in an inside-out patch with the presence or absence of Ca^{2+}, NC1, and PI(4,5)P_2 diC8 in the bath (cytosolic). NC1 and PI(4,5)P_2 diC8 were introduced after Ca^{2+} activation and desensitization due to Ca^{2+}-induced membrane PI(4,5)P_2 depletion. A-E mark the time points of hTRPM4 in various states: A, apo closed state; B, initial Ca^{2+}-activated state before desensitization; C, Ca^{2+}-bound desensitized state due to PI(4,5)P_2 depletion; D, closed state in the presence of NC1; E, NC1/PI(4,5)P_2-activated state. The panel on the right depicts sample I-V curves corresponding to A-E time points. **b** Similar recordings as **a** except that PI(4,5)P_2 diC8 was introduced before NC1, and the time point D marks the closed state in the presence of PI(4,5)P_2 diC8. The panel on the right depicts sample I-V curves corresponding to A-E time points. **c** Sample I-V curves of wild-type hTRPM4 and its alanine substitutions at the PI(4,5)P_2-binding site recorded in whole-cell patches with 10 μM NC1 in the bath (extracellular). **d** Outward and inward current densities of NC1-activated wild-type hTRPM4 and its mutants recorded at ±100 mV in whole-cell patches with 10 μM NC1 in the bath (extracellular). Bars represent mean ± SEM of n=5 independent replicates (shown as dots). p-values were calculated using a two-sided Student's t-test and are provided in the Source Data file. ** represents $p < 0.01$ and * represents $p < 0.05$.

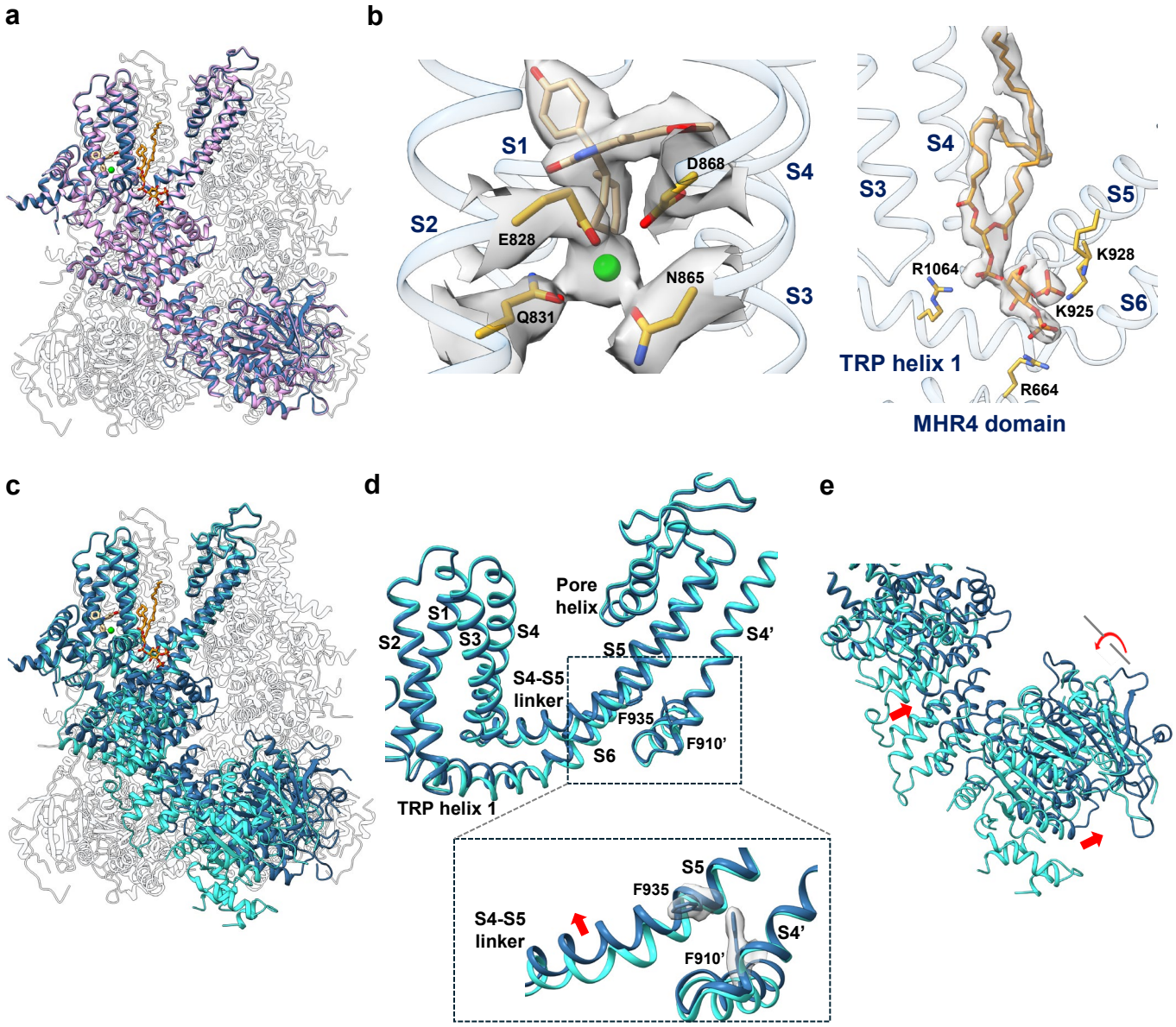

Fig. 5: Structure of NC1/PI(4,5)P_2-bound hTRPM4. a Superposition of the NC1/PI(4,5)P_2-bound and Ca^{2+}/PI(4,5)P_2-bound (PDB:9MRT) hTRPM4 open structures with the front subunits highlighted in navy blue and pink, respectively. NC1 and PI(4,5)P_2 are depicted in stick representation, and Ca^{2+} is shown as a green sphere. **b** Zoomed-in view of the ligand binding sites in the NC1/PI(4,5)P_2-bound structure. Ca^{2+} is represented as a green sphere. NC1, PI(4,5)P_2, and ligand-interacting residues are shown in stick representation. Density (grey surface) is contoured at 0.48 for NC1, Ca^{2+} and Ca^{2+} interacting residues and at 0.45 for PI(4,5)P_2 in ChimeraX. **c** Superposition of the NC1/PI(4,5)P_2-bound open and NC1-bound hTRPM4 structures with the front subunits highlighted in navy blue and cyan, respectively. **d** Enlarged view of the conformational changes at the transmembrane region between the NC1/PI(4,5)P_2-bound open (navy blue) and NC1-bound (cyan) structures. The S4 helix from the neighboring subunit (S4') is also shown. The inset shows a close-up highlighting the coupling between F935 and neighboring F910' in the NC1/PI(4,5)P_2-bound structure that leads to the movement (red arrow) at the S4-S5 linker and S5 and channel opening. Density for F935 and F910' is shown in a grey surface and contoured at 0.55 in ChimeraX. **e** Conformational changes at the cytosolic MHR domains between the NC1/PI(4,5)P_2-bound (navy blue) and NC1-bound (cyan) structures. Red arrows mark the upward swing of the cytosolic MHR domains and the rotation of MHRs 1 and 2.

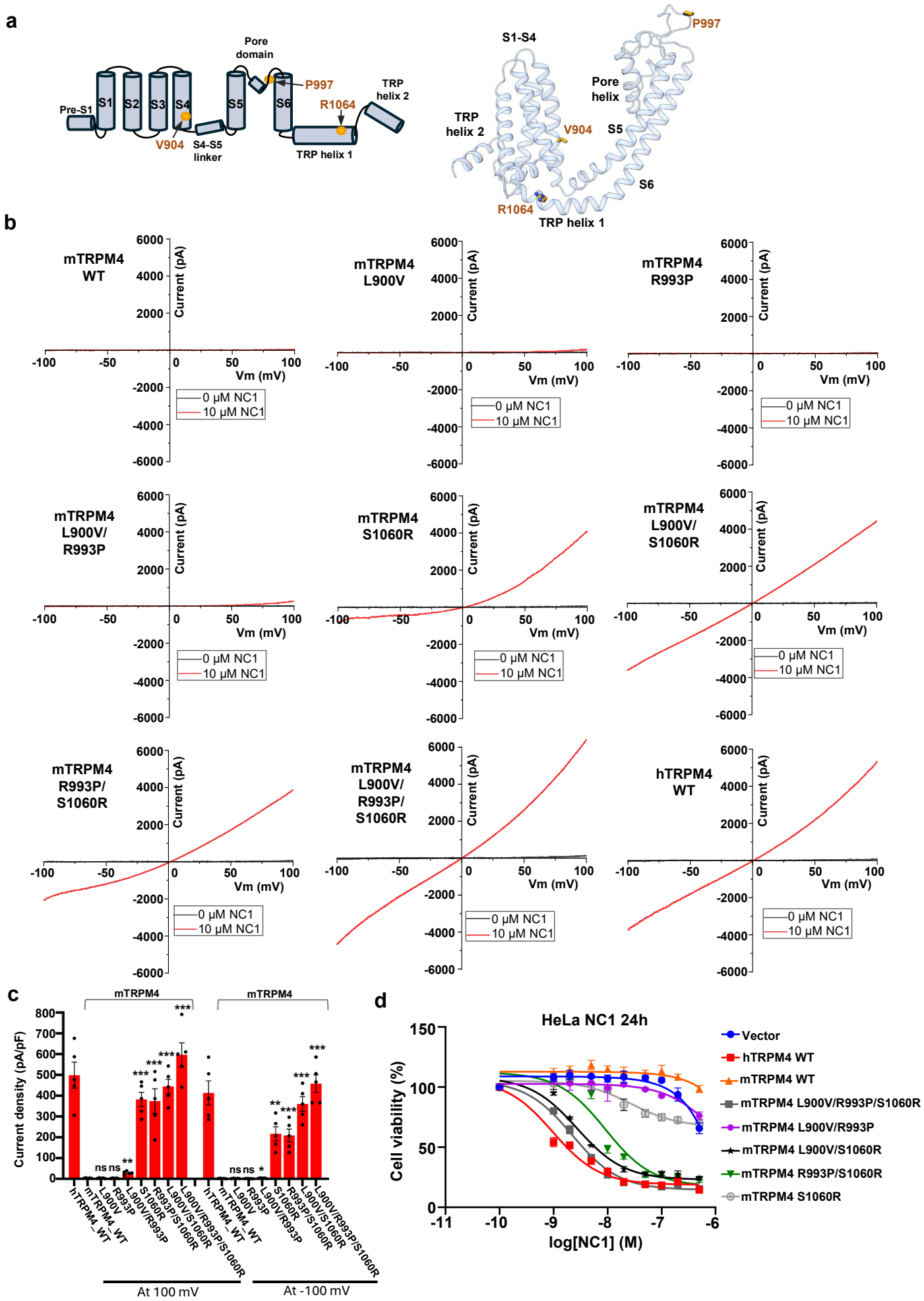
a
Pre-S1
S1
S2
S3
S4
S5
S6
Pore domain
P997
R1064
TRP helix 2
V904
S4-S5 linker
TRP helix 1
S1-S4
Pore helix
S5
S6
b
mTRPM4 WT
mTRPM4 L900V
mTRPM4 R993P
mTRPM4 L900V/ R993P
mTRPM4 S1060R
mTRPM4 L900V/ S1060R
mTRPM4 R993P/ S1060R
mTRPM4 L900V/ R993P/ S1060R
hTRPM4 WT
Current (pA)
Vm (mV)
0 μM NC1
10 μM NC1
c
mTRPM4
Current density (pA/pF)
hTRPM4_WT
mTRPM4_WT
L900V
R993P
S1060R
L900V/R993P
L900V/S1060R
R993P/S1060R
L900V/R993P/S1060R
At 100 mV
At -100 mV
d
HeLa NC1 24h
Cell viability (%)
log[NC1] (M)
Vector
hTRPM4 WT
mTRPM4 WT
mTRPM4 L900V/R993P/S1060R
mTRPM4 L900V/R993P
mTRPM4 L900V/S1060R
mTRPM4 R993P/S1060R
mTRPM4 S1060R

Fig. 6: Molecular determinants of NC1 specificity for human TRPM4. a Topology (left) and structure (right) of the hTRPM4 TM domain with the three key residues important for NC1 specificity marked. **b** Sample I-V curves of wild-type mTRPM4 and its single, double, and triple mutants at the three key residues. Currents were recorded in whole-cell patches with 10 μM NC1 in the bath (extracellular). Current from NC1-activated wild-type hTRPM4 is shown in the last panel for comparison. **c** Outward and inward current densities of the wild-type mTRPM4 and its mutants recorded at ±100 mV in whole-cell patches with 10 μM NC1 in the bath (extracellular). Bars represent mean ± SEM of n=5 independent replicates (shown as dots). p-values were calculated using a two-sided Student's t-test and are provided in the Source Data file. *** represents $p < 0.001$, ** represents $p < 0.01$ and * represents $p < 0.05$. Current densities of hTRPM4 are also graphed for comparison. **d** Dose-dependent NC1 cytotoxicity in stable HeLa cell lines expressing wild-type hTRPM4, wild-type mTRPM4, or mTRPM4 mutants. Data points represent mean ± SD of n = 3 independent replicates.

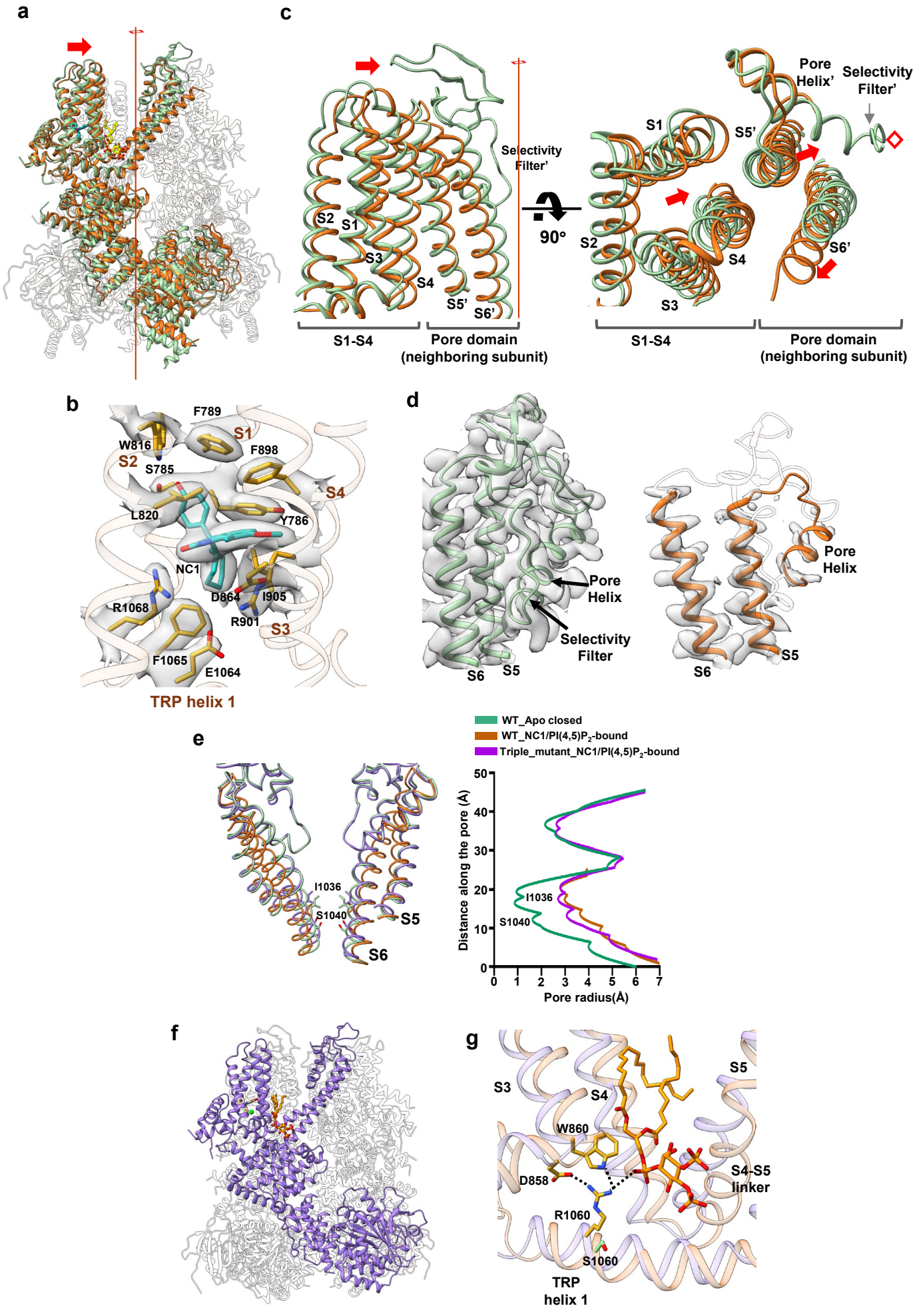
a
c
Selectivity Filter'
S2
S1
S3
S4
S5'
S6'
S1-S4
Pore domain (neighboring subunit)
90°
Pore Helix'
Selectivity Filter'
S1
S5'
S2
S4
S3
S6'
S1-S4
Pore domain (neighboring subunit)
b
F789
S1
W816
F898
S2
S785
S4
L820
Y786
NC1
D864
I905
R1068
R901
S3
F1065
E1064
TRP helix 1
d
Pore Helix
Selectivity Filter
S6
S5
Pore Helix
S5
S6
e
I1036
S1040
S5
S6
WT_Apo closed
WT_NC1/PI(4,5)P2-bound
Triple_mutant_NC1/PI(4,5)P2-bound
Distance along the pore (Å)
Pore radius(Å)
I1036
S1040
f
g
S3
S4
S5
W860
D858
S4-S5 linker
R1060
S1060
TRP helix 1

Fig. 7: NC1 binding in mTRPM4. a Superposition of the NC1/PI(4,5)P_2-bound (brown) and apo closed (PDB:6BCJ) (green) wild-type mTRPM4 structures along the pore axis, with the front subunits highlighted. NC1 (blue) and PI(4,5)P_2 (yellow) are shown in stick representation. **b** Zoomed-in view of the NC1 binding site in mTRPM4. NC1 and its surrounding residues are shown in stick representation. Density for NC1 and surrounding residues (grey surface) is contoured at 0.23 in ChimeraX. **c** Conformational changes at S1-S4 and its neighboring pore domain upon NC1 binding to mTRPM4. The red line and red diamond mark the central 4-fold axis. Red arrows indicate the major movements in this region, namely the lateral movement of S1-S4 towards the central axis, the inward movement of the neighboring subunit S5 (S5'), and the outward movement of the neighboring subunit S6 (S6'). **d** Comparison of the density maps at the pore domain between the apo closed (PDB:6bcj) (green) and NC1/PI(4,5)P_2-bound (brown) mTRPM4 structures. The disordered region in the pore domain of the NC1/PI(4,5)P_2-bound structure is depicted as a semi-transparent cartoon. **e** Structural comparison of the ion conduction pore in the apo closed (green), NC1/PI(4,5)P_2-bound inactivated (brown) wild-type mTRPM4 and in the NC1/PI(4,5)P_2-bound open (purple) triple mutant (L900V/R993P/S1060R). Gating residues I1036 and S1040 are shown in stick representation. The front and back subunits were removed for clarity. The panel on the right depicts the pore radius along the central axis in these structures. The dotted line illustrates the disordered filter region in the NC1/PI(4,5)P_2-bound wild-type mTRPM4. **f** Structure of the NC1/PI(4,5)P_2-bound mTRPM4 triple mutant (L900V/R993P/S1060R) with the front subunit highlighted in purple. NC1 and PI(4,5)P_2 are shown in stick representation and Ca^{2+} as a green sphere. **g** Structural comparison at S1060 region between NC1/PI(4,5)P_2-bound wild-type mTRPM4 (light brown) and its triple mutant (L900V/R993P/S1060R, light purple). PI(4,5)P_2 and key residues important for stabilizing S1-S4 in the mutant are shown in stick representation. The wild-type S1060 side chain is also shown for comparison.